Signatures of Eurasian heat waves in global Rossby wave spectra

Iana Strigunova, Richard Blender, Frank Lunkeit, and Nedjeljka Žagar

Meteorological Institute, Center for Earth System Research and Sustainability (CEN), Universität of Hamburg, Grindelberg 5, 20144 Hamburg, Germany

Correspondence: Iana Strigunova (iana.strigunova@uni-hamburg.de)

Abstract. This paper investigates systematic changes in the global atmospheric circulation statistics during Eurasian heat waves (HWs). The investigation of Rossby wave energy anomalies during heat waves HWs is based on the time series of Hough expansion coefficients representing Rossby waves with the troposphere-barotropic structures during the extended boreal summer in the ERA5, ERA-Interim, JRA-55, and MERRA reanalyses. The climatological Rossby-wave Rossby wave energy distribution is shown to follow a χ^2-distribution with skewness dependent on the zonal scale.

The heuristic approach applied multivariate decomposition reveals signatures of Eurasian surface heat waves on global energy spectra. It is shown that the skewness in planetary waves increases during Eurasian heat waves while the opposite occurs in the zonal mean flow. No change in the the Eurasian HWs on the probability density functions of the Rossby wave energy across scales. Changes in the PDFs are consistent with changes in the intramonthly variance during HWs. For the zonal mean state (the zonal wavenumber $k = 0$), a decrease in skewness is found, although not statistically significant. A decrease in skewness hints to an increase in synoptic-scale Rossby waves. Instead, synoptic zonal wavenumbers $k = 7-8$ are characterised by a statistically significantincrease of about 5% in the intramonthly variance with respect to the climatology. The largest increase of about 20% in the intramonthly variance is found in the zonal mean state asymmetrical Rossby wave with the meridional index 6 along with the decrease in the mode 4. This reflects the the number of active degrees of freedom indicating more independent modes involved in the circulation. A shift in the spectral distribution of the $k = 0$ intramonthly variance is shown to describe a weakening of the mean westerlies near their core at 45°N and their strengthening at higher latitudes around 75°N. At planetary scales ($k = 1-3$), the skewness in the troposphere-barotropic Rossby wave energy significantly increases. This coincides with a reduction of intramonthly variance, in particular for $k = 3$, and persistent large-scale circulation anomalies. At synoptic scales ($k = 4-10$), no change in skewness is detected for the Eurasian HWs. However, synoptic waves $k = 7-8$ are characterised by a statistically significant increase in intramonthly variance of about 5% with respect to the climatology. In addition, a shift of the entire Rossby wave energy distribution at synoptic scales, along with amplification, is observed during HWs.

Keywords: Eurasian heat waves, Rossby waves, global energy spectraspectral decomposition, circulation statistics, skewness, entropy, intramonthly variance

1 Introduction

Heat waves, periods with the daily maximum temperatures exceeding the climatological conditions by certain thresholds, have been increasing in numbers and magnitude, especially over Eurasia (e.g., Rousi et al., 2022). While the current operational numerical weather and ensemble prediction systems forecast such extremes several weeks ahead (e.g., Emerton et al., 2022), understanding the mechanism and dynamics of heat waves poses a challenge. Heat waves (HWs) are connected with persistent high-pressure systems (blockings). Numerous studies focus on the onset and drivers of blocking; however, no consensus exists due to complexity of dynamical and thermodynamical processes involved (e.g., Kautz et al., 2022). Blockings are often parts of large-scale quasi-stationary wave patterns (e.g., Stefanon et al., 2012). On one side, persistent weather patterns are part of internal variability. On the other side, the effect of climate change on the frequency and persistence of these patterns is still under debate (Woollings et al., 2018). For example, Park and Lee (2019) showed that these persistent weather patterns can be forced or triggered by remote anomalous tropical heating~~("tropical forcing")~~. While the physical mechanisms leading to blockings are under discussion (Petoukhov et al., 2013; Nakamura and Huang, 2018; Teng and Branstator, 2019; Wirth and Polster, 2021), the quasi-stationary behaviour of these wave patterns is shown to lead to concurrent extreme events (Kornhuber et al., 2020; Fuentes-Franco et al., 2022).

In contrast to previous studies investigating particular aspects of ~~heat waves~~HWs, our research aims to identify changes in the global ~~Rossby-wave circulation~~ Rossby wave energy statistics during Eurasian ~~heat waves~~HWs and to couple them to the observed circulation. While a number of studies addressed particular aspects of ~~heat waves~~ HWs over Eurasia (e.g., Feudale and Shukla, 2011; Schneidereit et al., 2012; Trenberth and Fasullo, 2012; Drouard and Woollings, 2018), their effects on the global ~~spatiotemporal~~ spatio-temporal variance spectra have not been studied. We analyze the global three-dimensional (3D) circulation ~~during Eurasian heat waves~~ in terms of horizontal and vertical scales of the Rossby waves and compare ~~it with the global circulation~~ the HWs with the climatology. As we show, the probability density function (PDF) of the ~~Rossby-wave circulation~~Rossby wave energy, which is described by the χ^2-distribution, changes during Eurasian ~~heat waves~~HWs. The changes are quantified by skewness ~~and entropy measures~~ of the PDFs for different zonal wavenumbers. The associated reduction of the number of active degrees of freedom compared to climatology can be used to explain the coarse structure of blocking events in the midlatitude troposphere.

The distributions of atmospheric fields are in general known to be non-Gaussian (Sura et al., 2005; Perron and Sura, 2013). However, the Central Limit Theorem may still be applicable when the sums of components in high-dimensional systems are involved, with assumptions of independent and identical distributions of summing components[1]. As we demonstrate, the distributions of anomalies in atmospheric energy can appear visually close to the normal distribution due to the Central Limit Theorem. However, the energy anomaly distributions are still skewed, which can be considered as an inherited property from energy (χ^2-distributions). The skewness, γ, of the χ^2-distribution is given by $\sqrt{8/df}$ and the excess kurtosis, κ, is given by $12/df$ with the number of independent degrees of freedom denoted df (Wilks, 2011). In the χ^2-distribution, the term "degrees

[1] Under the independence of components or variables in a high-dimensional system, one can consider that its time series are uncorrelated. The identity of distributions of summing components can be regarded in terms of their mean and variances being equal.

of freedom" is defined by the number of sum of squares of independent (uncorrelated) normally distributed variables. In our analysis, the number of degrees of freedom is the number of all possible modes used in the projection, while the number of active degrees of freedom is a measure of the concentration of energy in large wavenumbers during a heat wave. It is important that localized structures like blocking do not consist of a finite set of low wavenumber modes but can also include contributions from higher wavenumbers (as is the case for Fourier series). Therefore, the number of active degrees of freedom is not a sharp condition but can be used to measure the system's complexity. Note that because the atmospheric circulation is the composite of the zonal mean state and the superposition of waves which might be dependent, the statistical properties might deviate from the ideal situation.

Advanced statistical methods are common tools in the research of extreme weather events. For example, Galfi and Lucarini (2021) analyzed surface heat waves HWs using Large Deviation Theory and found that the associated persistent atmospheric patterns are not typical (in the statistical sense) compared to the climatology but follow a dynamics which is already encoded in the natural climate variability. Lucarini and Gritsun (2020) considered blockings as manifestations of Unstable Periodic Orbits and their stability as an indicator of predictability and the involved number of degrees of freedom. They find low predictability at the onset and the decay, and increased predictability in the mature phase of blocking events in the Atlantic.

A more common tool for the examination of midlatitude circulation during heat waves is the Fourier series analysis of single variable data along the latitude circles. This approach identifies anomalies in the planetary- and synoptic-scale Rossby waves during extreme events in terms of the Fourier amplitudes and phases of temperature, geopotential or wind variables at different levels. For example, Screen and Simmonds (2014) found a significant increase in the monthly variance and mean of anomalies of the Fourier amplitudes of 500 hPa geopotential heights for zonal wavenumbers 3-8 and suggested that amplified planetary waves are connected with temperature and precipitation extremes. Coumou et al. (2014) analyzed wind fields at 300 and 500 hPa and found out that zonal wavenumbers $6-8$ are the most probable candidates for quasi-resonance (amplified quasi-stationary Rossby waves due to the resonance with free waves trapped within the waveguide) according to Petoukhov et al. (2013). More recently, Kornhuber et al. (2019) showed the coupling between the zonal wavenumber 7 in daily wind and temperature data at several standard pressure levels and surface extremes, such as heat waves HWs and floods which occurred during the boreal summer 2018.

Our heuristic approach to spectral analysis of heat waves HWs considers the horizontal and vertical scales simultaneously by using the normal-mode function (NMF) decomposition to project daily circulation fields onto Rossby and non-Rossby components (Kasahara, 2020). The NMF decomposition is multivariate meaning that the wind and geopotential variables are represented by the same spectral expansion coefficient thereby separating the circulation into the balanced (or Rossby) and unbalanced (non-Rossby) components[2].

Previous applications of the NMF decomposition showed that modal analysis complements other methods of analysing global circulation by providing scale- and dynamical regime dependent information on the variability and by quantifying it in wavenumber space (Žagar et al., 2017, 2020, 2019). Žagar et al. (2020) quantified amplitudes and trends in midlatitude

[2]The real-time decomposition of the ECMWF circulation in Rossby and non-Rossby components is available on the MODES webpage https://modes.cen.uni-hamburg.de.

traveling and quasi-stationary Rossby waves and in the equatorial wave activity in the reanalysis data. They found a statistically significant reduction of subseasonal variance in Rossby waves with zonal wavenumber $k = 6$ along with an increase in variance in wavenumbers ~~$k = 3\breve{}5$~~ $k = 3 - 5$ in the summer seasons of both hemispheres. However, they did not attempt to relate these changes with the surface weather or extreme events. This task is carried out in the present study.

Our goal is to investigate whether and how surface heat waves during boreal summer over Eurasia affect the global atmospheric variability spectrum. While it is not evident *a priori* that regional ~~heat waves~~ HWs have their signatures in the global Rossby wave spectra, we show that this is, in fact, the case. First, we demonstrate statistically significant changes in the global total energy anomalies ~~PDFs during heat waves~~probability density functions (PDFs) during HWs. Then, we interpret the dynamics of the planetary Rossby waves through the change in active degrees of freedom and show its relation with the entropy reduction during Eurasian ~~heat waves~~HWs.

The paper is organized as follows. The 3D decomposition method, statistical analysis and the heat waves identification algorithm are explained in Section 2. Section 3 contains results. First, we present examples of the NMF decomposition for two recent ~~heat waves~~HWs. This is followed by the results of statistical analysis of spatial spectra (climatological and ~~heat waves~~ HWs energies) and its interpretation by filtering parts of balanced circulation back to physical space. Finally, we discuss how temporal variance spectra change during ~~heat waves~~HWs. Conclusions are presented in Section 4.

2 Method and Data

In this section we describe our research method that makes use of the NMF decomposition and the MODES software (Žagar et al., 2015). The method is applied to the four modern reanalysis datasets. We present the criteria for Eurasian surface ~~heat waves~~ HWs and associated selection method for the spectral expansion coefficients.

2.1 Normal-mode function decomposition of global circulation

The NMF decomposition is carried out in the terrain-following, global coordinate system $(\lambda, \varphi, \sigma)$, where ~~$\sigma$~~ $\sigma = p/p_s$ is the ratio of the vertical level pressure p and the surface pressure p_s, λ denotes longitude and φ is latitude. At every time step t, the horizontal winds (u, v) and geopotential height (h) on σ levels are projected to precomputed vertical and horizontal structure functions (VSFs and HSFs, respectively). The VSFs are the numerical solutions of the vertical structure equation whereas the HSFs are eigensolutions of the Laplace equation without forcing and are given in terms of the Hough harmonics. The Hough harmonics are defined as a product of the latitude-dependent Hough functions and harmonic waves in the longitudinal direction (e.g. Kasahara, 2020). The horizontal and vertical structures are coupled by the eigenvalues of the vertical structure equation, the so-called "equivalent depth"~~which is also the mean depth of the linearized shallow-water equations~~. The reader is referred to Žagar et al. (2015) and Kasahara (2020) and references therein for details of the theory.

~~MODES is applied to the four modern reanalyses: ERA5 (Hersbach et al., 2020), ERA-Interim (Dee et al., 2011), the Japanese 55-year Reanalysis JRA-55 (Kobayashi et al., 2015), and the Modern-Era Retrospective analysis for Research and Applications MERRA (Rienecker et al., 2011). We use daily data at 12 UTC from 1980-2014 (1980-2019 for ERA5) on the regular Gaussian~~

grid that consists of 256 × 128 grid points in the zonal and meridional directions, respectively. Vertically the data are interpolated on the predefined 43 σ levels.

The projection The projection of discrete data consists of two steps. In the first step, the 3D data $\mathbf{X}(\lambda,\varphi,\sigma)$ data vector $\mathbf{X}(\lambda,\varphi,\sigma) = (u,v,h)^{\mathrm{T}}$ is expanded into a series of orthogonal VSFs denoted G_m according to

$$\mathbf{X}(\lambda,\varphi,\sigma) = (u,v,h)^{\mathrm{T}} = \sum_{m=1}^{M} G_m(\sigma)\,\mathbf{S}_m\,\mathbf{X}_m(\lambda,\varphi)\,. \tag{1}$$

The vertical mode index m ranges from 1 to M, the total number of vertical modes, that can be equal or less the number of vertical levels. For every m, the nondimensional data matrix $\mathbf{X}_m(\lambda,\varphi) = (\tilde{u},\tilde{v},\tilde{h})^T$ is obtained by the normalisation by the 3×3 diagonal matrix $\mathbf{S}_m$ with elements $\sqrt{gD_m}$, $\sqrt{gD_m}$, D_m, where D_m denotes the equivalent depth of the vertical mode m. The nondimensional variables are defined with ~denoted with $\tilde{()}$.

In the second step, the horizontal nondimensional motions are projected onto a series of Hough harmonics $\mathbf{H}_n^k$ for every m as

$$\mathbf{X}_m(\lambda,\varphi) = \sum_{n=1}^{R}\sum_{k=-K}^{K} \chi_n^k(m)\,\mathbf{H}_n^k(\lambda,\varphi;m)\,, \tag{2}$$

where K denotes the total number of zonal waves and R is the total number of meridional modes. The complex Hough expansion coefficients $\chi_n^k(m)$ depend on three indices: m, meridional mode index n and zonal wavenumber k. For every n, the projection includes two types of motions: Rossby modes[3] (quasi-geostrophic or balanced dynamics) and inertia-gravity modes that represent divergence-dominated unbalanced dynamics. The inertia-gravity modes consist of eastward- and westward-propagating solutions and together with the equatorial Kelvin and mixed Rossby-gravity waves constitute the non-Rossby modes that are not used in this study.

It is the inverse of Eq. (1) and Eq. (2) that is solved in the forward projection. The second step gives the complex Hough expansion coefficients $\chi_n^k(m)$ as

$$\chi_n^k(m) = \frac{1}{2\pi}\int_0^{2\pi}\int_{-1}^{1} \mathbf{X}_m(\lambda,\varphi)\,[\mathbf{H}_n^k]^*\,\mathrm{d}\mu\,\mathrm{d}\lambda\ .\,, \tag{3}$$

The integration where $\mu = \sin(\varphi)$ and the asterisk (*) denotes the complex conjugate. The integrations in the zonal direction is and meridional directions are calculated by the fast Fourier transform and in meridional direction by the Gaussian quadrature, respectively.

The MODES is applied to the four modern reanalyses: ERA5 (Hersbach et al., 2020), ERA-Interim (Dee et al., 2011), the Japanese 55-year Reanalysis JRA-55 (Kobayashi et al., 2015), and the Modern-Era Retrospective analysis for Research and Applications MERRA (Rienecker et al., 2011). We use daily data at 12 UTC from 1980-2014 (1980-2019 for ERA5) on the regular Gaussian grid that consists of 256 × 128 grid points in the zonal and meridional directions, respectively. Vertically the data are interpolated on the predefined 43 σ levels. The same datasets and setup were used in Žagar et al. (2020) except that

[3] We use both 'modes' and 'waves' interchangeably but the latter refers to the case without the zonal mean state ($k = 0$).

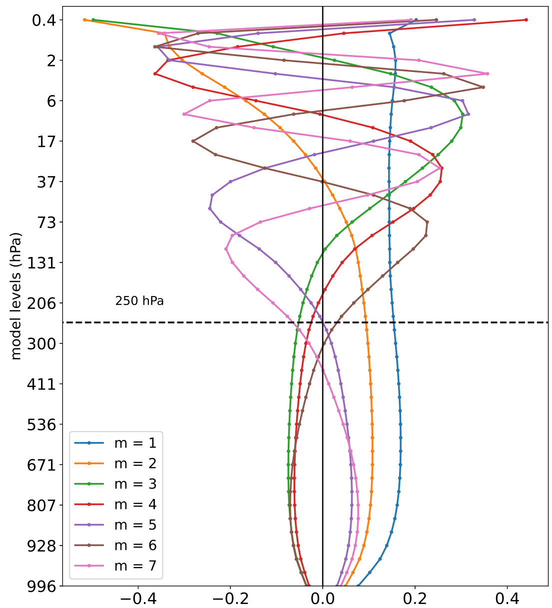

Figure 1. Vertical structure functions (VSFs) for the first seven vertical modes. VSFs are derived for 43 σ levels using the stability profile of ERA-Interim data. VSFs that do not change the sign below the tropopause (defined as 250 hPa level) are troposphere-barotropic modes.

ERA5 has been extended for the period 2015-2019. The projection is carried out using the following truncations: $K = 100$, $M = 27$, and $R = 150$ which combines 50 meridional modes for the Rossby modes, for the eastward inertia-gravity and for westward inertia-gravity waves modes. Since the mixed Rossby-gravity mode is counted as the first balanced modes, ~~we have~~ the present study makes use of 49 Rossby modes for every m and k, ~~so that~~ with the meridional mode index ~~goes~~ going from $n = 1$ to $n = 49$.

We are interested in the balanced circulation with the troposphere-barotropic vertical structure that characterises the midlatitude weather during ~~heat waves. As shown in Fig. 1, the first five VSFs~~ HWs. This is taken into account by selecting a subset of the VSFs that do not change their signs within the tropopause. In the NMF decomposition, the rigid lid is at zero pressure, just like in the models used for reanalyses. The 43-level datasets extend vertically up to about 0.5 hPa so that a number of VSFs is characterised by a barotropic structure within the troposphere meaning no zero crossing below the tropopause~~(~~. The first seven VSFs are shown in Fig. 1. With the middle latitude tropopause taken at 250 hPa~~), and can therefore~~ , the VSFs with $m = 1-5$ can be regarded as troposphere-barotropic modes. ~~Vertical structure functions (VSFs) for the first seven vertical modes. VSFs are derived for 43 σ levels using the stability profile of ERA-Interim data. VSFs that do not change the sign below the tropopause (defined as 250 level) are troposphere-barotropic modes.~~

2.2 Heat Waves

~~We analyze heat waves for~~ The study area is the Eurasian region limited by the Ural mountains [35°N-65°N, 10°W-60°E]. The study area is frequently affected by ~~heat waves~~ HWs (e.g., Zhou and Wu, 2016), in particular, Eastern Europe and Western Russia, a ~~region~~ location of one of the strongest ~~heat waves~~ HWs observed in recent decades (e.g., Barriopedro et al., 2011). For heat wave identification, we analyze daily 2 m temperature fields for the extended boreal summer (months May to September, denoted MJJAS) from 1980-2014 (until 2019 for ERA5). The identification algorithm ~~applied by Ma and Franzke (2021) uses~~ of Ma and Franzke (2021) applies the following two criteria: (i) the temperature exceeds the 95th percentile threshold and (ii) the duration of the exceedance is ~~larger~~ longer than three consecutive time steps ~~.~~ (three days). Table 1 presents the list of days with HWs in the four reanalysis datasets, which is based on the algorithm. As the identification algorithm is performed independently for each reanalysis, it is expected to have discrepancies among them ~~. Table 1presents the list of days with heat waves in reanalysis datasets~~ as seen in Table 1. Thirteen HWs are identified in ERA-Interim, ~~which is based on the algorithm mentioned above~~JRA-55 and MERRA but the duration of HWs in individual datasets differ. Note that there are two cases with a shorter duration (2 days instead of 3 days) that were included to recognise that the four reanalyses reproduce the same HW events. All together, there are 537 days with HWs that is about 1.5% of the total number of days, a percentage expected for extreme events.

2.3 Time series of Rossby wave energy anomalies

~~The total (kinetic plus available potential) energyof a single mode~~ Our statistics makes use of Rossby wave energy anomalies during HWs in comparison to the climatology. We compute the energy time series, their anomalies and standard deviations used for standardisation, followed by combining standardised time series for all troposphere-barotropic modes and statistical analysis. In the first step, the total energy (the kinetic energy plus the available potential energy) is computed for every circulation mode ν, $\nu = (k, n, m)$~~is given by~~ , as the square of the absolute value of the ~~Hough coefficient (i.e. in terms of its real and imaginary parts) as~~ complex Hough expansion coefficient χ_ν:

$$I_\nu = I_n^k(m) = \frac{1}{2} g D_m \left| \chi_n^k(m) \right|^2 , \tag{4}$$

where g is the gravity. ~~See Kasahara (2020) for~~ For the derivation of Eq. (4), see Kasahara (2020) or Kasahara and Puri (1981)
.

The time series of the daily total energy~~is denoted~~ , $I_\nu(t)$, span over the ~~period of extended boreal summer (MJJAS , May-September)~~ MJJAS period within 35 years (1980-2014) for ERA-Interim, JRA-55, MERRA ($N_y = 35$) and 40 years (1980-2019) for ERA5 ($N_y = 40$). The climatological annual cycle is ~~obtained~~ defined as an average over all years (N_y) for each day in MJJAS as

$$\langle I_\nu \rangle = \frac{1}{N_y} \sum_{y=1}^{N_y} I_{\nu,y} , \tag{5}$$

Table 1. Heat waves in Eurasia during May-September 1980-2019

		ERA5	ERA-Interim	JRA-55	MERRA
	Start date	Number of detected days			
1	1994-09-23	3	3	2	3
2	2006-06-18	12	10	12	10
3	2006-09-20	3	5	6	2
4	2007-05-20	12	12	12	12
5	2007-08-21	6	6	6	6
6	2008-09-05	4	3	4	3
7	2010-06-28	26	27	27	26
8	2010-07-27	21	21	19	21
9	2012-05-09	4	4	4	4
10	2012-06-14	4	3	4	3
11	2013-05-02	7	7	6	5
12	2014-05-17	5	3	3	3
13	2014-06-05	5	6	5	6
14	2015-06-02	3	-	-	-
15	2015-08-11	3	-	-	-
16	2015-09-17	11	-	-	-
17	2016-06-21	4	-	-	-
18	2016-08-20	9	-	-	-
19	2018-05-02	8	-	-	-
20	2018-06-27	4	-	-	-
21	2018-07-13	22	-	-	-
22	2018-08-29	7	-	-	-
23	2018-09-11	12	-	-	-
24	2019-06-01	3	-	-	-
25	2019-06-08	5	-	-	-
26	2019-06-18	3	-	-	-
27	2019-06-23	4	-	-	-
28	2019-07-24	3	-	-	-
$\sum$days		213	110	110	104

and subtracted from daily energies to compute the energy deviations (or anomalies) as

$$I'_\nu = I_\nu - \langle I_\nu \rangle \,. \tag{6}$$

The time series of I'_ν define the climatology.

At this stage, we form also the time series of energy anomalies with time steps of the observed ~~heat waves~~ HWs according to Table 1. ~~Although only 13 heat waves are identified in ERA-Interim, JRA-55 and MERRA due to the shorter datasets, we include them to increase the sample size. We note that all 13 heat waves are identified in all reanalyses, but the individual datasets differ, as can be inferred from the number of detected days. Thus, we consider them as different realizations. We normalize~~ We divide energy anomalies by their climatological standard deviation σ_ν,

$$\tilde{I}'_\nu = \frac{I'_\nu}{\sigma_\nu} \,. \tag{7}$$

The mode-wise normalisation by the standard deviation (i.e. standarisation in mathematical sense) is crucial since the energy spectrum is red not only in terms of the horizontal scales (Žagar et al., 2017), but also in terms of the vertical scale. Note that the entire time series of energy anomalies (climatology) and time series during ~~heat waves~~ HWs are normalized by different σ. This procedure is applied for every reanalysis ~~dataset~~ independently.

The next step is to split the ~~normalized~~ normalised energy anomalies of the single Rossby modes into planetary ($k = 1-3$) and synoptic ($k = 4-10$) ~~intervals, and then~~ scales, and to average over the five troposphere-barotropic modes~~$m = 1-5$ within these intervals~~. The mean zonal flow ~~is given~~ defined by $k = 0$ is analysed separately. For each k, averaging is applied also over meridional modes whenever the results are discussed in terms of ~~a single modal index.~~

the zonal wavenumber. Finally, we combine the time series of ~~normalized energy anomalies in the above-mentioned wavenumber ranges~~the normalised energy anomalies from the four reanalyses in the three subdomains of the global circulation: the zonal mean state, the planetary and the synoptic waves. Žagar et al. (2020) showed that the differences between climatological ~~energy~~ variance spectra for the four reanalyses are minor. Therefore, our PDFs consist of independent but similar time series. Thus, we can detect robust features of distributions of energy anomalies across different datasets.

3 Results

~~First, Fig. 2 demonstrates~~ Our presentation of the results starts by showing that the selected Rossby modes from the NMF decomposition and the applied HW detection method correspond to the circulation patterns typical for the HW events. After demonstrating our methodology, we continue with the statistical analysis of the Eurasian HWs in global spectra and wrap up by coupling statistical properties with the circulation changes during HWs. But first we demonstrate in Fig. 2 that the global energy in a single Rossby mode is χ^2-distributed~~.~~[4]. The presented example uses the energy I_ν (Eq. 4) of the Rossby mode with ~~$(k,n,m) = (7,3,1)$~~ $\nu = (k,n,m) = (7,3,1)$ which is associated with variability in midlatitude barotropic circulation. The histogram and the fit of the χ^2-distribution with two degrees of freedom, $df = 2$, correspond to the real and the imaginary parts of the time series of $I_n^k(m) = I_3^7(1)$. The Kolmogorov-Smirnov test reveals a negligible p-value, confirming the fit. Therefore, we find that approximation of χ^2-distributed energy is satisfied to a high degree, as expected.

[4] The Greek letter χ used for the statistical distribution is not related to our Hough expansion coefficient χ_ν, the notation of which follows Žagar et al. (2015).

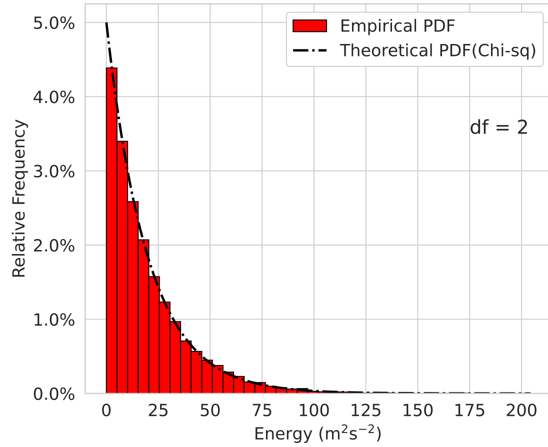

Figure 2. Atmospheric energy (empirical) distribution in the Rossby wave with the zonal wavenumber $k = 7$, meridional mode $n = 3$ and vertical index $m = 1$ for 1980-2014. The dashed black lines correspond to the theoretical ~~(~~χ^2 ~~)~~distribution (df are the degrees of freedom).

3.1 Northern Hemisphere midlatitude circulation during heat waves

~~In this section,~~ Now we demonstrate that the selected subset of vertical modes is suitable for the statistical analysis ~~by demonstrating the climatological circulation~~ of HWs by showing the climatological state and two selected ~~heat wave eventswith applied filtering. We show the ERA5 results, but other datasets provide similar results.~~ events. Figure 3a depicts the May-September balanced wave circulation (Rossby modes with $k > 0$ and all m, n) at ~~a single~~ σ level close to 500 hPa. The pattern remains almost the same when ~~we restrict vertical modes to~~ only the troposphere-barotropic vertical modes, $m = 1-5$, are retained (Fig. 3b). This confirms ~~that~~ our selection of ~~modes is suitable for analyzing the troposphere-barotropic circulation, i. e. the patterns observed during surface extreme events commonly associated with the blocking.~~

the VSFs. Figure 3 is based on the ERA5 results, but other datasets provide similar results.

~~This structure is clearly recognized when we reconstruct~~ The circulation during the Eurasian HWs is commonly associated with the blocking and can be in the NMF-filtered circulation during two recent ~~extreme heat~~ HW events: the Russian Heat Wave in 2010 (Barriopedro et al., 2011) shown in Fig. 3c and the European Heat Wave in 2019 (Xu et al., 2020) ~~,~~ displayed in Fig. 3e. The difference with respect to climatology ~~which is presented~~ in Fig. 3b ~~. In both cases, we observe strong positive anomalies over the locations of the observed surface~~ are seen in greatly enhanced amplitudes of the anticyclonic circulation over the observed surface temperature extremes (Western Russia and Europe)~~with nearby negative anomalies~~. For the Russian Heat Wave in Fig. 3c, d, ~~the anomalies over Central and Southern Asia reveal cyclones which have produced extreme rainfall known as~~ anomalies over Asia have been coupled to the Pakistan Flood (Lau and Kim, 2012). ~~Furthermore~~Similar, the wavy pattern along the latitudinal belt depicts teleconnections (Teng and Branstator, 2019). The ~~plots with the~~ difference between climatology and ~~each heat wave~~ HWs (Fig. 3d,f) ~~demonstrate~~ shows the meridional extension of the ~~waves from polar to tropical~~

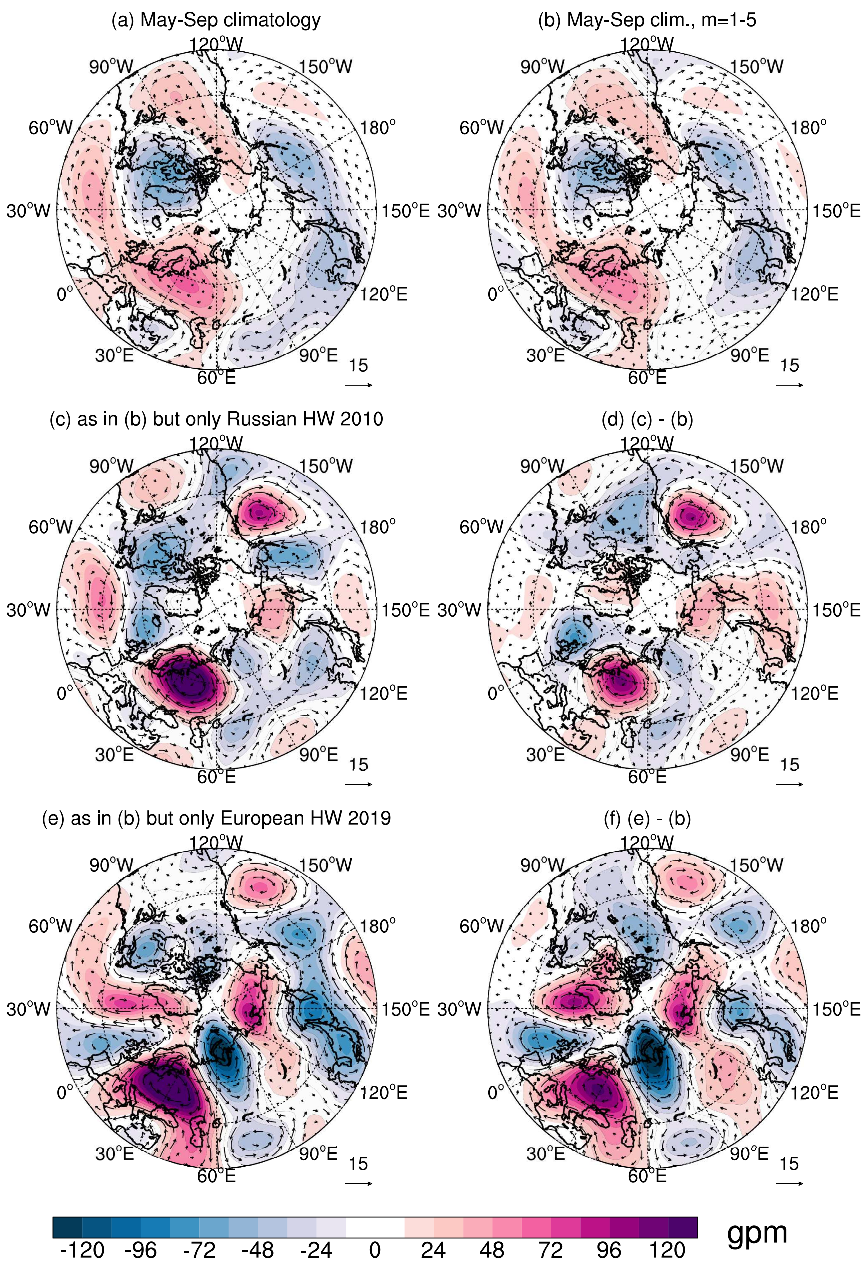

Figure 3. (a,b) Climatological Rossby wave circulation for extended boreal summer (MJJAS) at σ level close to 500 hPa ~~(ERA5 model level 30)~~ in the midlatitudes~~(35°N - 65°N)~~. ~~Coloured contours are geopotential height anomalies (in) for Rossby waves and (~~a) ~~zonal~~ Zonal wavenumbers $k > 0$~~(no zonal mean state)~~, all meridional modes n and all vertical modes m~~-,~~ . (b) as in (a), but only troposphere-barotropic vertical modes, $m = 1 - 5$~~,~~ . (c) ~~as~~ As in (b) but for the Russian Heat Wave (HW) in ~~2010.~~ 2010, and (d) ~~Difference~~ difference between the (c) and (b). (e) As in (~~e~~b), and (~~e,~~ f) ~~illustrate Rossby waves during~~ as in (d) but for the European ~~Heat Wave (~~HW ~~)~~ in 2019. ~~Wind~~ Coloured contours are geopotential height anomalies (in gpm), and the wind speed is shown by the length of the wind vectors (15 $\mathrm{m/s}^{-1}$ as a reference vector).

~~regions confirming the impact~~ circulation anomalies from the tropics to the polar regions in agreement with the suggested coupling of these regions ~~on~~ during midlatitude extremes (Behera et al., 2012). ~~While~~ Overall, the patterns shown in Fig. 3 are qualitatively known from previous studies~~, our result was obtained by a novel method that allows a~~. The novelty is that our results are produced by multivariate filtering of the global 3D circulation allowing a scale-dependent quantification of the ~~associated circulation with respect to the global climatology. This result also justifies our use of the subset of vertical modes in the statistical analysis presented below.~~ circulation and anomalies associated with extreme events.

3.2 ~~Statistics~~ Global statistics in ~~modal~~ Rossby-wave space: climatology

~~The example in the previous section demonstrated how the Rossby circulation is altered regionally during Eurasian heat waves.~~ Our next step is to investigate how ~~these heat waves~~ the Eurasian HWs affect (if) the global spatial variability spectrum, i.e. their impact on global circulation. Here, the term global variability spectrum refers to the PDFs of the ~~normalized~~ normalised anomalies in global energy, ~~and~~ whereas the effects (or signatures) of ~~heat waves implies~~ HWs imply significant changes in the distribution of energy anomalies. ~~As a first step, we analyze the climatological PDFs in terms of~~ The climatological PDFs are analysed for zonal wavenumbers corresponding to three ranges as described in Section 2: (i) the zonal mean state, $k = 0$, (ii) the planetary-scale circulation $k = 1-3$, and (iii) the synoptic-scale circulation with $k = 4-10$. We focus on the skewness which is not impacted by the ~~normalization~~normalisation.

Figure 4a shows the PDF ~~with~~ for the case when all zonal wavenumbers are included in the analysis. With the skewness equal to 0.38, the PDF clearly deviates from a Gaussian distribution. ~~The planetary-scale (Fig. 4c) and the synoptic-scale~~ A deviation from the normal distribution is found for all three wavenumber ranges considered (Fig. 4~~d)PDFs also do not follow a normal distribution, but~~ b-d). All three exhibit noticeable asymmetry, with the zonal mean and planetary-scale skewness almost twice greater than the one of the synoptic-scale Rossby waves. In addition, we note that the distributions for the zonal mean and the planetary-scale are broader than for the synoptic-scale. This may reflect that the variability of the larger scales involves more time scales with a larger range of magnitudes.

The ~~skewness of the PDFs~~ robustness of the statistical analysis in Fig. ~~4 is based on the four reanalyses (ERA5, ERA-I, JRA-55, MERRA) combined. We apply bootstrapping with a replacement for different wavenumber ranges for a more robust statistical analysis (Fig. 5). Note that all values from reanalysis datasets are~~ 5 is checked by applying bootstrapping with replacement for skewness and excess kurtosis with 1000 realizations for every presented wavenumber range. All results are found to be within the defined 95% confidence intervals (CI) for each wavenumber range (~~here is~~ not shown). The bootstrapped skewness also shows that the ~~normalized~~ normalised energy anomaly distribution has the highest asymmetry in the planetary scales and the zonal mean circulation ~~which is also detected as stretched~~ seen as extended right tails in the PDFs ~~. The different number of single~~ in Fig. 5. The different numbers of contributing modes can partly explain the different skewnesses in the four wavenumber ranges. However, changes in the dynamics, such as during HWs, can modify the skewness and the active degrees of freedom, ~~which is addressed in the nextsection~~as discussed next.

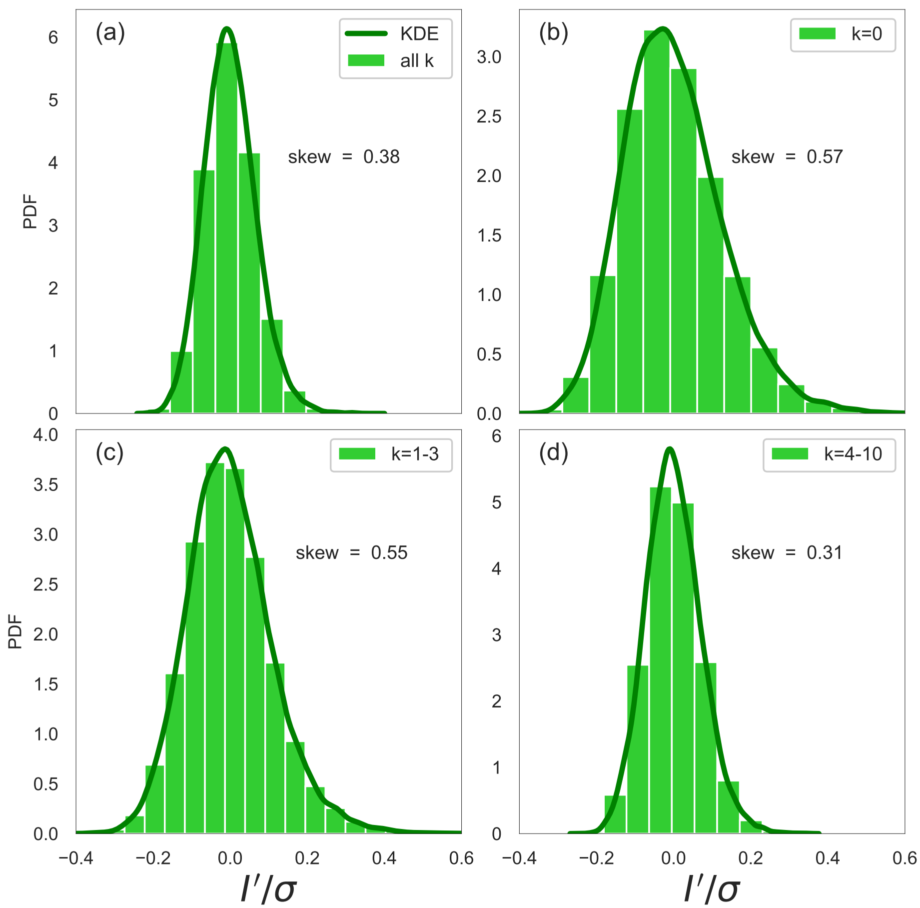

Figure 4. PDFs of ~~normalized total~~ the normalised energy anomalies in the global balanced (Rossby mode) circulation for (a) all k~~)~~, (b) the zonal mean state ($k = 0$), (c) planetary-scale waves ($k = 1-3$), (d) synoptic-scale waves ($k = 4-10$). ~~Empirical~~ The empirical PDFs are depicted as green bars~~for extended boreal summer (MJJAS) 1980-2014 (1980-2019 for ERA5)~~. The ~~blue~~ dark green curve is the Kernel Density Estimator (KDE).

3.2.1 ~~Surface extremes and~~ Changes in the Rossby-wave energy statistics during heat waves

Now we compare PDFs during ~~observed heat waves~~ the observed HWs over Eurasia with ~~climatology for different parts of wavenumber space. For comparison, we consider two statistical moments,~~ the climatology in terms of the skewness and excess kurtosis ~~, to~~ that diagnose the changes in shape, especially in the tails of distributions~~for the four reanalyses datasets. We find~~

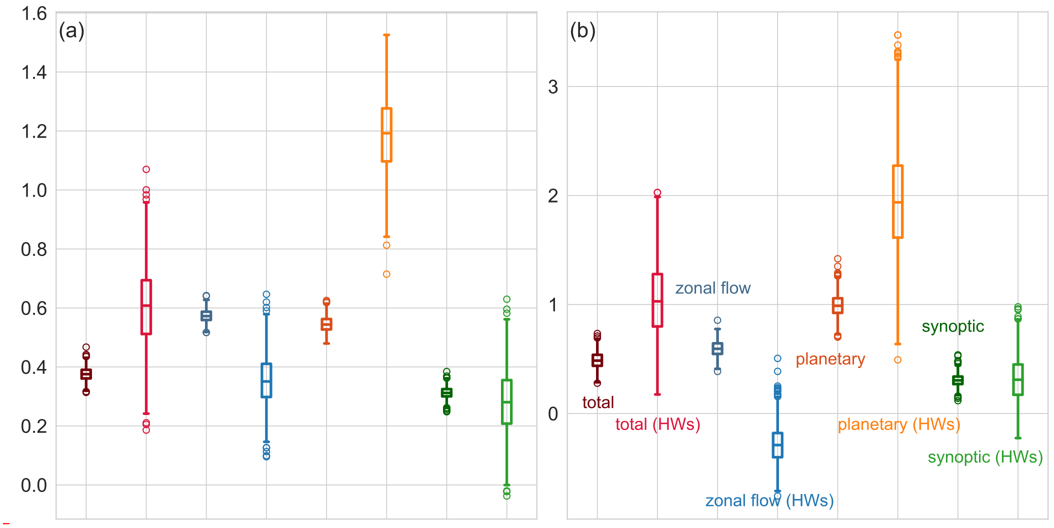

Figure 5. Box-plots for the (a) skewness and (b) excess kurtosis of normalized the PDFs of normalised energy anomalies distributions for four considered atmospheric circulation components: total Rossby regime with balanced flow (dark- and light-red bars), the zonal mean balanced flow as ($k = 0$, dark- and light-blue bars), planetary planetary-scale Rossby waves as ($k = 1-3$, orange and yellow bars), and the synoptic circulation as synoptic-scale Rossby waves ($k = 4-10$, dark- and light-green bars). Vertical lines mark 95%-confidence intervalsare obtained through bootstrapping with replacement with 1000 simulations. Darker and lighter shades denote the climatology and HWs, respectively.

that only the difference in the skewness of the planetary-scale distribution is statistically significant, i.e the bootstrapped values are outside CIs of climatological bootstrapped skewness only during extremes. .

The PDFs of the normalized energy anomalies depicted normalised energy anomalies in Fig. 6 demonstrate how probabilities of the energy deviations change during surface extreme events. First, there is aHWs. For the normalized total energy anomalies (all k; Fig. 6a) the PDF becomes broader with a longer positive tail indicating more high energy extremes. For the zonal mean flow ($k = 0$; Fig. 6b) only small changes are visible on the first view. The PDF of the planetary waves ($k = 1-3$; Fig. 6c) shows a shift of the maximum towards negative values and more positive values. While the aforementioned changes of the entire PDFs are not significant, we identify a statistically significant change (according to the Mann-Whitney U test with 95%-confidence) in the PDFs of synoptic Rossby waves ($k = 4-10$; Fig. 6d). Here, the complete distribution is shifted to higher values without change in its shape. The shift can be interpreted as increased positive shift in the mean except for $k = 0$, and , as a consequence, an increased probability of intermediate positive deviations . deviations in the synoptic-scale energy during HWs. More energy in synoptic-scale circulation can be viewed as more intensive cyclones and anticyclones which are found to maintain blocking by eddy straining (Shutts, 1983) and selective absorption (Yamazaki and Itoh, 2013) mechanisms.

According to Fig. 5a , the change in How do the skewness and the excess kurtosis change during Eurasian HWs? An increase (decrease) in skewness hints to less (more) active degrees of freedom, which can be interpreted as less (more) independent

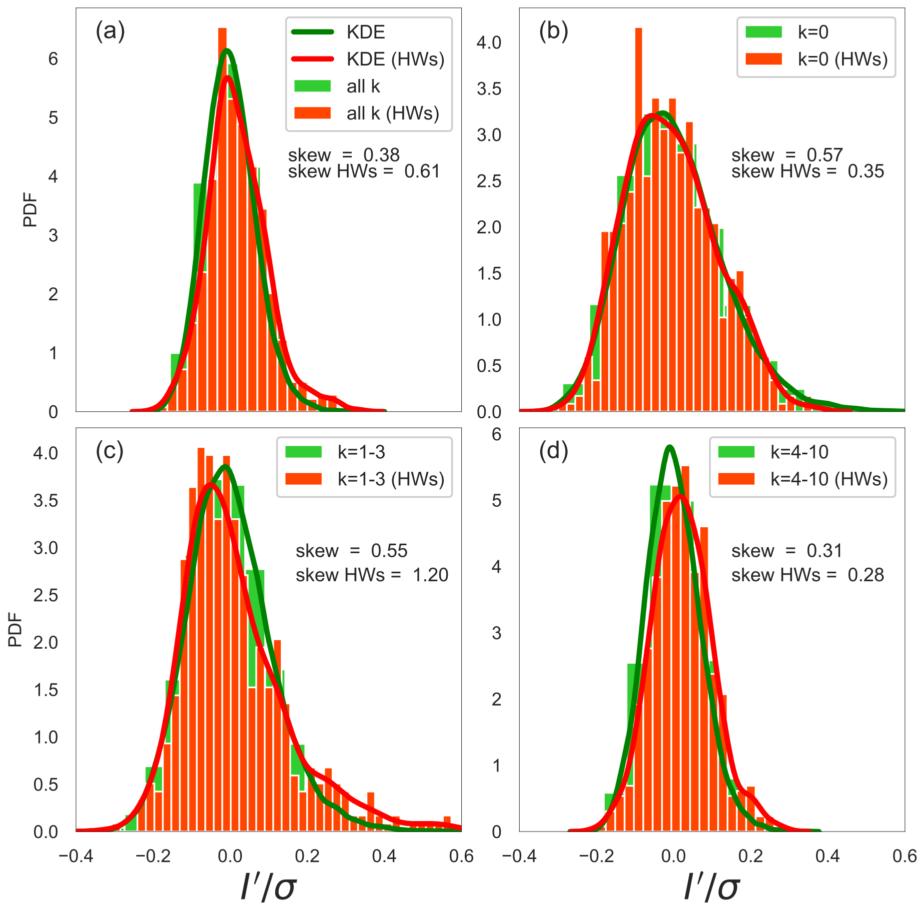

Figure 6. ~~The same as~~ As in Fig. 4, but ~~with normalized energy anomalies only during~~ for the Eurasian heat waves ~~(HWs) presented~~ listed in Table 1.

modes contributing to the variability. This can be caused by both a change in the number of contributing modes and a change of temporal coherence between different modes contributing. An increase of excess kurtosis reflects a rise in the probability of extreme values.

Figure 5 shows the skewness and the excess kurtosis for both the climatology and the HWs. For HW events, the ~~skewness, which is considered as the main indicator, is the largest for the planetary-scale circulation. The~~ two quantities change in qualitatively the same way for different ranges of the wavenumbers. While we find almost no changes for the synoptic waves, changes are the largest at the planetary scales (Fig. 5b). In this case, the excess kurtosis for extreme events is approximately twice larger than climatology~~(Fig. 5b)~~, which reflects a ~~drastic~~ rise in the probability of extreme values. The opposite change is found for the zonal mean flow~~during surface heat waves~~, where skewness and the excess kurtosis decrease; this implies that the distribution becomes flatter with thinner tails and is less extreme. ~~Based on this, we conclude that the amplitudes of the planetary circulation amplify~~ We conclude that anomalies of the planetary-scale circulation show relatively less (and more coherent) variability in general and persistent anomalies are generated as shown in Fig. 3d, f, ~~while the~~ although positive extremes are more likely. On the other hand, the zonal mean flow anomalies become in general weaker in agreement with Coumou et al. (2014). ~~Thus, we have evidence that signatures of heat waves are seen in different parts of the global variability spectrum via statistically significant changes in skewness.~~

The ~~increase~~ change in skewness allows for the estimation of the ~~reduction of~~ change in the active degrees of freedom during the ~~heat waves~~ HWs compared to the ~~climatological mean~~climatology. For the estimation, we use the exact relation for the skewness of χ^2-distributed variable, $\gamma = \sqrt{8/df}$, where df is the number of squares of the independent Gaussian variables with a unit variance which defines the χ^2-distributed variable.

~~We use the ratio~~ We use $df_e/df_c = \gamma_c^2/\gamma_e^2$, which says that the ratio between the number of active degrees of freedom during ~~heat waves~~ HWs and climatology, df_e and df_c respectively, is equal to the ratio of their skewnesses γ_e and γ_c, respectively. ~~The rough estimates~~ For the planetary waves which shows the largest change, the estimated $\gamma_e \approx 1.2$ and $\gamma_c \approx 0.6$ ~~, based on Fig.5a,~~ (see Fig. 5a) yield a reduction of the active degrees of freedom of ~~the order of $df_e/df_c \approx 1/4$ during the extreme events~~about 25% during HWs.

~~Unlike the change in skewness in the PDFs of the planetary Rossby waves, there is a statistically significant change (according to the Mann-Whitney U test with 95%-confidence) in the entire PDFs of synoptic Rossby waves. The change can be seen in a distribution shift toward positive energy anomalies (figure not shown), which can be interpreted as more energy is expected at synoptic scales during heat waves. More intensive cyclones and anticyclones are found to maintain blocking throughout eddy straining (Shutts, 1983) and selective absorption (Yamazaki and Itoh, 2013) mechanisms.~~

Finally, we make a note on the fact that the changes in PDFs during the Eurasian ~~heat waves~~ HWs apply to the global atmosphere. Our Rossby modes consist of symmetrical (n odd) and asymmetrical (n even) components with symmetry with respect to the equator defined for the geopotential height and zonal wind fields. We checked that both symmetrical and asymmetrical parts contribute to the PDFs of all meridional modes. In other words, the Rossby waves in the Southern Hemisphere might have contributed to the results presented. However, taking into account the lower frequency of atmospheric blocking (Wiedenmann et al., 2002) in the Southern Hemisphere, we may assume that this influence is negligible.

3.3 Changes in the midlatitude barotropic planetary-scale circulation during heat waves

The next step is to relate the PDFs of energy anomalies in large-scale circulation with physical space. This is achieved by filtering the analyzed Rossby modes ($k = 1 - 3, n = 1 - 49, m = 1 - 5$) changes in the PDFs for different scales can be physically interpreted by filtering selected Rossby waves to physical space, similar to what has been done in Fig. 3. Instead of case studies, now we present the planetary-scale circulation averaged over all days with observed extremes. As earlier, we show the horizontal circulation at ERA5 σ-level near 500 hPa as representative for the troposphere-barotropic circulation.

Figure 7a is very similar to Fig.3b which included all zonal wavenumbers. Figures 7band c reveal an enhancement of positive height anomalies in the eastern part of the Baltic Sea and negative anomalies ,c reveal that during the Eurasian HWs, a large enhancement of the positive geopotential height anomaly over Northern Europe and a negative geopotential anomaly over the North Atlantic . Moreover, one can notice a north-westward shift of negative anomalies in the Asian part compared to climatology presented in Fig. 7a and the formation of positive anomalies over Chukotka and Alaska. According to Fig. 7c, the dominant patterns are zonal wavenumber 2 and 3.

Figures 7d,e show the vertical profile for central Asia takes place. The vertical cross sections along the latitude circle 54°N of the meridional wind speed and the geopotential height anomalies for climatology, during heat waves. Figure 7f depicts the difference between two profiles. We illustrate again that the structure is barotropic over the entire troposphere and lower stratosphere , as was observed in some studies.Moreover,there is an enhancement of reveals the expected troposphere-barotropic vertical structure of anomalous circulation that extends throughout the lower stratosphere (Fig. 7d,e). The northward winds over Europe (0°E -30°E) and southward winds over the Asian part of Russia (60°E -90°E) with southerlies over the Kamchatka Peninsula (Fig. 7f). are enhanced during HWs. Overall, we find an increase in wave amplitudes, and change in phases as can be noticed by west- and northward shifts in Fig. 7b,c and Fig. 7d,e in the Baikal lake area $(90^\circ E - 120^\circ E)$. According to The results in Fig. 7 align with Teng and Branstator (2012) and Ragone and Bouchet (2021), the wave-3 pattern is dominant for heat waves where the zonal wavenumber $k = 3$ pattern was found dominant for HWs that occurred in the US, France and Scandinavia. Therefore, the results demonstrate how atmospheric circulation is changed that changes in atmospheric circulation during surface extremes not only locally occur not only regionally but also in remote regions, similar to the idea of teleconnection patterns noted in recent studies (e.g., Kornhuber et al., 2019).

3.4 Intramonthly Changes in intramonthly variance and entropy reduction during the surface heat waves

So far, we showed signatures of heat waves discussed signatures of HWs in spatial variance (energy). Now we look at investigate related changes in temporal variance due to extremes and couple it to the changes in entropy which measures the average uncertainty with which one knows the state of the systemon intramonthly scales. The temporal variance and its square root, variability, are usually studied locally at single points or using the time series of atmospheric indices such as North Atlantic Oscillation. The global intraseasonal variance in the reanalysis data was analyzed was analysed by Žagar et al. (2020) who showed statistically significant trends in both midlatitude Rossby waves and in large-scale equatorial waves. Here, we

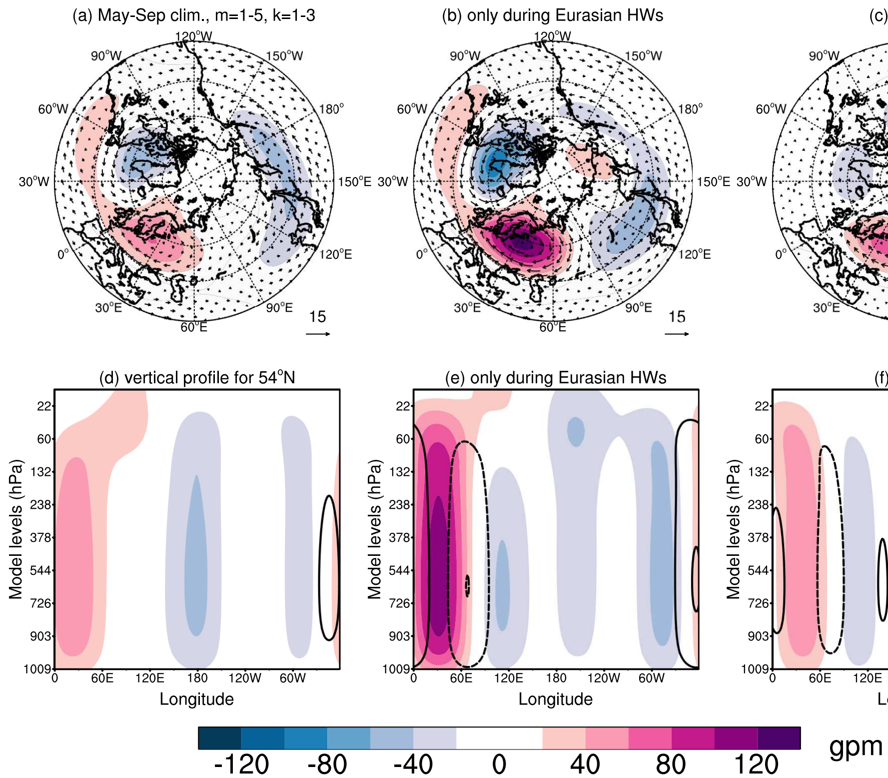

Figure 7. Planetary-scale, troposphere-barotropic Rossby waves ($k = 1-3$, $m = 1-5$, all n) at the σ — σ level close to 500 hPa in ERA5. Coloured contours are geopotential height anomalies, every 20 . The wind speed is shown by the arrow length. (a) Mean circulation in May-September obtained in the 40-year climatology (1980-2019), (b) composite of 28 Eurasian Heat Waves (HWs) presented in Table 1, (c) difference between (b) and (a). Coloured contours are geopotential height anomalies, every 20 gpm. The wind speed is shown by the arrow length. (d)Climatological -(f) Longitude-pressure cross sections of planetary-scale geopotential height perturbations (coloured colours) and meridional wind (isolines) in planetary scales perturbations along 54°N. (d) Climatology, (e) As in (d) but during HWs, (f) difference between (d) and (e). Solid and dashed contours in (d)-(f) show correspond to the planetary-scale meridional winds (northward and southward meridional wind speed, respectively), , every 2 ms^{-1}.

focus on intramonthly scales associated with heat waves with the compare the climatological intramonthly variance with that for the months with the observed Eurasian HWs in all reanalyses.

The unbiased variance (Jkg^{-1}) is computed as

$$V_\nu = \frac{1}{N-1}\sum_{t=1}^{N} gD_m |\chi_\nu(t) - \overline{\chi}_\nu|^2 , \tag{8}$$

where $\overline{\chi}_\nu$ is the monthly mean and N is the number of days in a single month. As the 3D NMF expansion is a complete representation of the system, the components ν of the state vector are statistically independent and correspond to independent degrees of freedom, as discussed in Section 2. The relative change in variance during heat waves is thus

$$\frac{(V_\nu - V_\nu^h)}{V_\nu} \quad \text{or} \quad 1 - \frac{V_\nu^h}{V_\nu},$$

where V_ν^h is the intramonthly variance during the heat waves. To obtain the mean state, variances are averaged over months May to September and years 1980 to 2019 in ERA5. For extremes, we consider intramonthly variances for months with observed heat waves. Zonal zonal wavenumber variance spectra of V_ν and V_ν^h are obtained by summing over the five barotropic vertical modes and over all meridional indices of the Rossby waves.

The entropy, $\mathcal{H}$, which measures the average uncertainty of the system, is defined as

$$\mathcal{H}(\mathcal{P}) = \int_{R^n} \mathcal{P}(\mathbf{x}) \ln(\mathcal{P}(\mathbf{x}))\, \mathrm{d}\mathbf{x} ,$$

where probability density $\mathcal{P}(\mathbf{x})$ represents the uncertainty of the state $\mathbf{x}$ of the system. The change in entropy can be described by the difference in entropy between the heat wave and climatological probability densities that are represented by diagonal matrices $\mathbf{Q}^{\mathrm{h}}$ the variances in the five vertical and $\mathbf{Q}$ with entries equal to V_ν^h and V_ν, respectively (Rogers, 2000). The change can be shown to be all meridional modes as previously. Intramonthly variance is computed for all months and averaged to create the climatological variance spectrum, V_ν. The averaging over all months with heat waves gives us the HW variance spectrum V_ν^h (Here we drop extra signs for the averaging operator). The relative change in intramonthly variance due to HWs is

$$\Delta\mathcal{H}(\mathcal{P}) = \mathcal{H}(\mathcal{P}^h) - \mathcal{H}(\mathcal{P}) = \frac{1}{2}\frac{V_\nu^h - V_\nu}{V_\nu} \quad \text{or} \quad \frac{V_\nu^h}{V_\nu} - 1 \ln\det(\mathbf{Q}^{\mathrm{h}}) - \frac{1}{2}\ln\det(\mathbf{Q}) = \frac{1}{2}\ln\det(\mathbf{Q}^{\mathrm{h}}\,\mathbf{Q}^{-1}). \tag{9}$$

The results are summarized global intramonthly Rossby wave variance spectrum is shown in Fig.8. First we discuss the intramonthly variance spectra shown in Fig. 8a. The overall red spectrum makes it hard to notice that scale-dependent differences 8a. It is a red spectrum, similar to the r subseasonal variance spectra in Žagar et al. (2020). The redness of the spectra in Fig. 8a makes differences between the climatology and HWs difficult to detect, but they are made clear by zooming in the planetary and synoptic scales displayed as an inset panel. It shows a variance reduction of about 6% in the zonal wavenumber $k = 3$ along with the 5% variance increase in $k = 7-8$. We note that the changes in intramonthly variance are consistent with the shifts of the maxima of the respective normalized energy anomaly PDFs (Fig. 6c,d). In addition, the reduction of planetary wave intramonthly variance is also consistence with the appearance of the persistent large-scale anomaly shown in Fig. 7.

The blue shading around the variance spectra in Fig. 8a depicts the 95%-CI obtained through bootstrappingof intramonthly variances. The largest uncertainty is at zonal wavenumbers for the planetary Rossby waves and it shows that the . It suggests the largest uncertainty at planetary zonal wavenumbers. The variance reduction at $k = 3$ is within 95%-CI and, therefore, is insignificant. The opposite is found at At $k = 7-8$, where the change in the the intramonthly variance during heat waves is significant. HWs is slightly outside of the CI; therefore, the variance change is considered significant. We note here that our findings are based on a relatively small sample of identified HWs and that many events lasted under a week. To provide stronger evidence, GCM simulations can be performed, which is the scope of the future studies.

Figure 8a however does not include the mean zonal state. A more detailed view of the changes in the global intramonthly variance in comparison with entropy during HWs is provided in other two panels. The variance reduction (Fig.8b) and the entropy reduction (Fig. 8c) are qualitatively very similar; they both show a decrease in Fig. 8b including also the mean zonal state. The variance reduction at $k = 3$ along with an increase in and an increase at $k = 7-8$. They also agree about the largest variance and entropy changes being are seen across multiple meridional modes n in agreement with the midlatitude character of HWs. The quantitatively largest variance change is however seen in the zonal mean state $k = 0$ with a positive and negative change in the two asymmetrical meridional modes, $n = 4$ and $n = 6$, respectively.

The change in $k = 0$ during Eurasian heat waves can be associated with physical space can be explained using the latitudinal structure of the Hough functions. But, perhaps even more insightful is the latitudinal profile of the zonal-mean zonal wind presented in Fig.9. Figure 9 9. First, it shows that the maximum zonal-mean zonal wind at 45°N during heat waves is weaker (HWs is about 10%) with respect to weaker than the climatology and slightly shifted (about 1°) northward. The wind maximum is also better confined within jet near 45°N is more confined in the troposphere, with the 10 ms^{-1} isoline at level close near 300 hPa compared to level close 200 hPa in climatology. The barotropicity of the midlatitude atmosphere near 45°N, as defined by the VSFs not changing the sign below 250 hPa but still supporting the This means that the vertical shear of the mean zonal wind , is decreased decreases during the Eurasian heat waves. HWs.

Another features of the heat waves HWs seen in Fig. 9 are twice stronger zonal-mean zonal winds in higher latitudes the latitude belt between 60°N and 90°N with a peak difference of up to 3 ms^{-1} at 75°N. The dipole shape of the difference in Fig. 9c is in Hough space of Fig.8b,c seen as an entropy decrease in Fig. 8b seen as a variance decrease in the meridional mode $n = 4$ and an increase in $n = 6$. Note that Fig. 9 is obtained by filtering $\overline{\chi}_n^0$ to physical spacethe $\overline{\chi}_n^0$ and that similar . Similar filtering for any horizontal or vertical scale of interest is straightforwardmaking , which makes the holistic modal-space statistics an attractive global complement to the single-variable, single-level Fourier analysis. We speculate that the enhancement of high latitude $k = 0$ zonal winds is a component of more-persistent double jets over Eurasia during heat waves HWs recently discussed by Rousi et al. (2022).

[4] The latitudinal profiles of the Hough functions for the Rossby waves with $n = 1-4$ are available at .

~~a) Time-averaged intramonthly variance spectra of the Rossby waves for climatology (blue line) and Eurasian heat waves (magenta line). Averaging is performed over a 40-year period 1980-2019, months May-Sep of ERA5. The embedded figure includes (bottom left) the percentage of relative change and (top right) zoomed spectra for $k = 6 - 9$. The 95%-confidence intervals (blue shading) are obtained through bootstrapping with replacement with 1000 simulations. b) Reduction in the intramonthly variance as a function of the zonal wavenumber starting with the zonal mean state, c) As in b), but the reduction in entropy multiplied by a factor of 2.~~

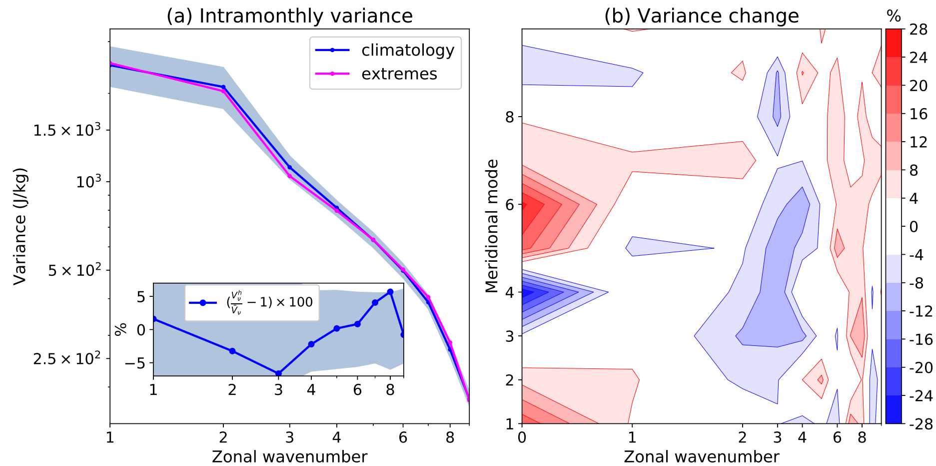

Figure 8. (a) Intramonthly variance spectra of Rossby waves for the climatology (blue) and Eurasian heat waves (magenta). The embedded figure shows the relative change in percentages of the climatology. The blue shading denotes the 95%-confidence intervals. (b) Changes in the intramonthly variance as a function of the zonal wavenumber including the zonal mean state.

4 Conclusions

Extreme events ~~like heat waves at the surface~~ such as surface HWs are accompanied by changes in atmospheric circulation across many scales. Our study shows that Eurasian ~~heat waves~~ HWs have signatures in the global balanced circulation. The changes in global statistics of the ~~Rossby wave~~ Rossby-wave variance are made evident by analyzing the four modern reanalyses: the ERA5, ERA-Interim, JRA-55, and MERRA datasets. The Rossby waves are identified by a multivariate projection of the global horizontal winds and geopotential height on the eigensolutions of the linearized primitive equations on the sphere with a basic state at rest (the so-called normal-mode functions). A complete projection basis provides global statistics of Rossby waves as a function of the zonal wavenumber, the meridional mode index and the vertical modes associated with the vertical structure functions~~that are barotropic~~. The method includes scale-selective multivariate Rossby-wave filtering in physical space offering an attractive global complement to the single-variable, single-level Fourier analysis.

Our analysis focuses on the Rossby waves with the barotropic structure within the troposphere ~~.~~

that is characteristic of the midlatitude circulation during HWs. The reconstructed physical space picture of the Eurasian ~~heat waves~~ HWs is in agreement with previous studies (Lau and Kim, 2012; Behera et al., 2012; Coumou et al., 2014; Teng and Branstator, 2019). ~~The enhancement of the zonal mean state ($k = 0$) zonal winds in high latitude of the Northern Hemisphere is likely a component of more-persistent double jets over Eurasia during heat waves recently discussed by Rousi et al. (2022). In modal~~

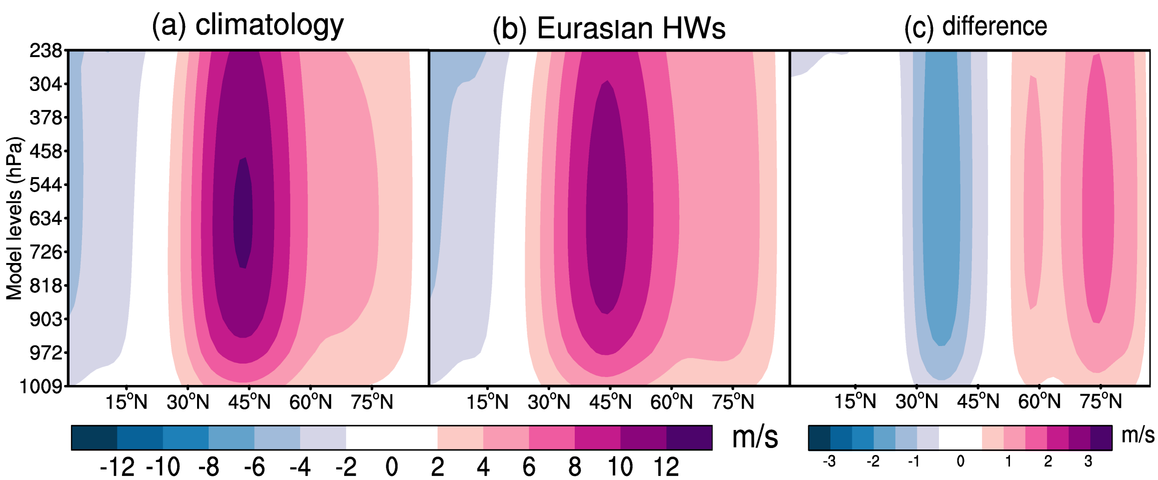

Figure 9. Zonal-mean zonal wind in the northern hemisphere troposphere in 1980-2019, May-Sep ERA5 data. (a) climatology, (b) Eurasian heat waves (HWs) and (c) climatology - ~~heat waves~~HWs.

~~space, this is seen as an increase of around 20% in the intramonthly variance in the zonal mean state asymmetrical Rossby mode with the meridional index 6 along with a similar decrease in the meridional mode 4. In physical space, the dipole-shaped change of the zonal-mean zonal wind is such that the~~ We find largely increased amplitudes of the positive geopotential height anomaly over Northern Europe, otherwise typical for the extended summer period, and a negative geopotential anomaly over the North Atlantic and central Asia. The anomalous circulation extends throughout the lower stratosphere. In addition, there are westward and northward shifts in the circulation. During HWs, the zonal mean westerlies somewhat weaken near their ~~core~~ climatological maximum at 45°N but get twice stronger in high midlatitudes (centred at 75°N). ~~A decreased barotropicity close to 45°N is interpreted as a reduced vertical shear of the mean westerly flow.~~ Future work should couple these findings with the study by Wirth and Polster (2021) on the role of Rossby waves in processes leading to the double jet formation, recently discussed for Eurasian HWs by Rousi et al. (2022).

The statistical analysis is carried out on the complex time series of the Hough expansion coefficients representing Rossby modes across many horizontal scales with the troposphere-barotropic ~~structures. We show~~ vertical structure. We demonstrate that the energy distribution of a single mode follows a χ^2-distribution. Statistics of the ~~normalized~~ normalised energy anomalies shows that the zonal mean state ($k = 0$) and the planetary-scale ($k = 1 - 3$) circulation are more skewed than the synoptic and smaller scales, with extended right tails. Increased skewness of the distribution hints to the reduction in active degrees of freedom. This can be interpreted as less independent modes contributing to the observed variability, either because the number of total modes is smaller or because there is temporal coherence between different modes.

During the Eurasian ~~heat waves~~HWs, the skewness in ~~planetary~~ planetary-scale waves increases while the opposite occurs in the zonal mean ~~flow~~state. The increase in skewness can be linked with a decrease in the number of active degrees of freedom during ~~heat waves~~HWs. This aligns with the results of Lucarini and Gritsun (2020) which are based on the atmospheric stability during Atlantic blockings. Based on the χ^2-skewness, we estimate a reduction of the active degrees of freedom during Eurasian ~~heat waves~~ HWs of about 25% compared to climatology.

Consistent changes in wavenumber space are found in the intramonthly variance~~and entropy. Eurasian heat waves~~. Eurasian HWs are characterised by a statistically significant increase of about 5% in the intramonthly variance at synoptic scales $k = 7-8$, with respect to climatology. This is consistent with increased synoptic activity during blocking (e.g., Shutts, 1983; Yamazaki and Itoh, 2013). In contrast, a reduction of intramonthly variance in $k = 3$ of about 6% is found not to be statistically significant. Future studies with longer datasets, such as climate model outputs are an opportunity for models' validation and larger datasets of extreme events.

Despite the uncertainties due to the limited sample size, our results provide the following overall picture consistent with previous studies. During HWs, planetary Rossby waves are less active (especially $k = 3$), and a persistent anomaly, typically referred to as blocking, is formed by waves less independent from each other. On the other hand, the variability of the synoptic Rossby waves increases, particularly at zonal wavenumbers $k = 7-8$. The contributions of more active meridional modes to the zonal mean flow during HWs, perhaps excited by eddy-mean flow interactions, lead to a shift or a double maximum in midlatitude mean westerlies.

Code and data availability. The ERA-Interim and ERA5 reanalysis datasets are available via http://www.ecmwf.int. The MERRA and JRA-55 are available at https://gmao.gsfc.nasa.gov/reanalysis/MERRA and https://jra.kishou.go.jp/JRA-55, respectively. The MODES software can be requested via https://modes.cen.uni-hamburg.de. The time series of the Hough expansion coefficients for the four reanalyses are available upon the request from the authors.

Author contributions. All authors contributed to the study conception and design. IS developed the algorithm, performed the data analysis and wrote a first draft of the manuscript. All authors participated in data interpretation and revised previous versions of the manuscript. All authors read and approved the final manuscript.

Competing interests. The authors declare that the research was conducted in the absence of any commercial or financial relationships that could be construed as a potential conflict of interest.

Acknowledgements. This work was funded by the Deutsche Forschungsgemeinschaft (DFG, German Research Foundation) under Germany's Excellence Strategy – EXC 2037 'CLICCS - Climate, Climatic Change, and Society' (CLICCS, A6) – Project Number: 390683824, contribution to the Center for Earth System Research and Sustainability (CEN) of Universität Hamburg. We thank the former MODES group members at the University of Ljubljana Damjan Jelić and Khalil Karami for the MODES decomposition of the four reanalysis data, to Žiga Zaplotnik for his advice on processing the Hough coefficients in Python, to Qiyun Ma for the algorithm for the heat ~~waves~~ wave identification and to Frank Sielmann for the variance analysis and technical support. We would also like to thank Valerio Lucarini for the discussion, and to two anonymous reviewers and Editor Dr. Gwendal Riviére for their constructive comments on the manuscript.

References

Barriopedro, D., Fischer, E. M., Luterbacher, J., Trigo, R. M., and García-Herrera, R.: The Hot Summer of 2010: Redrawing the Temperature Record Map of Europe, Science, 332, 220–224, https://doi.org/10.1126/science.1201224, 2011.

Behera, S. K., Ratnam, J. V., Masumoto, Y., and Yamagata, T.: Origin of extreme summers in Europe: the Indo-Pacific connection, Clim. Dyn., 41, 663–676, https://doi.org/10.1007/s00382-012-1524-8, 2012.

Coumou, D., Petoukhov, V., Rahmstorf, S., Petri, S., and Schellnhuber, H. J.: Quasi-resonant circulation regimes and hemispheric synchronization of extreme weather in boreal summer, Proc. Natl. Acad. Sci. U.S.A., 111, 12 331–12 336, https://doi.org/10.1073/pnas.1412797111, 2014.

Dee, D. P., Uppala, S. M., Simmons, A. J., Berrisford, P., Poli, P., Kobayashi, S., Andrae, U., Balmaseda, M. A., Balsamo, G., Bauer, P., Bechtold, P., Beljaars, A. C. M., van de Berg, L., Bidlot, J., Bormann, N., Delsol, C., Dragani, R., Fuentes, M., Geer, A. J., Haimberger, L., Healy, S. B., Hersbach, H., Hólm, E. V., Isaksen, L., Kållberg, P., Köhler, M., Matricardi, M., McNally, A. P., Monge-Sanz, B. M., Morcrette, J.-J., Park, B.-K., Peubey, C., de Rosnay, P., Tavolato, C., Thépaut, J.-N., and Vitart, F.: The ERA-Interim reanalysis: configuration and performance of the data assimilation system, Q. J. R. Meteorol. Soc., 137, 553–597, https://doi.org/10.1002/qj.828, 2011.

Drouard, M. and Woollings, T.: Contrasting mechanisms of summer blocking over western Eurasia, Geophys. Res. Lett., 45, 12–040, https://doi.org/10.1029/2018GL079894, 2018.

Emerton, R., Brimicombe, C., Magnusson, L., Roberts, C., Di Napoli, C., Cloke, H. L., and Pappenberger, F.: Predicting the unprecedented: forecasting the June 2021 Pacific Northwest heatwave, Weather, n/a, https://doi.org/https://doi.org/10.1002/wea.4257, 2022.

Feudale, L. and Shukla, J.: Influence of sea surface temperature on the European heat wave of 2003 summer. Part I: an observational study, Clim. Dyn., 36, 1691–1703, https://doi.org/10.1007/s00382-010-0788-0, 2011.

Fuentes-Franco, R., Koenigk, T., Docquier, D., Graef, F., and Wyser, K.: Exploring the influence of the North Pacific Rossby wave sources on the variability of summer atmospheric circulation and precipitation over the Northern Hemisphere, Clim. Dyn., pp. 1–15, https://doi.org/10.1007/s00382-022-06194-4, 2022.

Galfi, V. M. and Lucarini, V.: Fingerprinting Heatwaves and Cold Spells and Assessing Their Response to Climate Change Using Large Deviation Theory, Phys. Rev. Lett., 127, 058 701, https://doi.org/10.1103/PhysRevLett.127.058701, 2021.

Hersbach, H., Bell, B., Berrisford, P., Hirahara, S., Horányi, A., Muñoz-Sabater, J., Nicolas, J., Peubey, C., Radu, R., Schepers, D., et al.: The ERA5 global reanalysis, Q. J. R. Meteorol. Soc., 146, 1999–2049, https://doi.org/doi.org/10.1002/qj.3803, 2020.

Kasahara, A.: 3D Normal Mode Functions (NMFs) of a Global Baroclinic Atmospheric Model, Modal View Of Atmospheric Variability: Applications Of Normal-Mode Function Decomposition in Weather and Climate Research. N. Žagar and J. Tribbia, Eds., Springer, Mathematics of Planet Earth Series, Vol.8, 2020.

Kasahara, A. and Puri, K.: Spectral representation of three-dimensional global data by expansion in normal mode functions, Mon. Wea. Rev., 109, 37–51, 1981.

Kautz, L.-A., Martius, O., Pfahl, S., Pinto, J. G., Ramos, A. M., Sousa, P. M., and Woollings, T.: Atmospheric blocking and weather extremes over the Euro-Atlantic sector–a review, Weather Clim. Dynam., 3, 305–336, https://doi.org/10.5194/wcd-3-305-2022, 2022.

Kobayashi, S., Ota, Y., Harada, Y., Ebita, A., Moriya, M., Onoda, H., Onogi, K., Kamahori, H., Kobayashi, C., Endo, H., Miyaoka, K., and K., T.: The JRA-55 reanalysis: General specifications and basic characteristics, J. Meteorol. Soc. Jpn. Ser. II, 93, 5–48, https://doi.org/10.2151/jmsj.2015-001, 2015.

Kornhuber, K., Osprey, S., Coumou, D., Petri, S., Vladimir, P., and Stefan, R. and, G. L.: Extreme weather events in early summer 2018 connected by a recurrent hemispheric wave-7 pattern, Environ. Res. Lett., 14, 054 002, https://doi.org/10.1088/1748-9326/ab13bf, 2019.

Kornhuber, K., Coumou, D., Vogel, E., Lesk, C., Donges, J. F., Lehmann, J., and Horton, R. M.: Amplified Rossby waves enhance risk of concurrent heatwaves in major breadbasket regions, Nat. Clim. Change, 10, 48–53, https://doi.org/10.1038/s41558-019-0637-z, 2020.

Lau, W. K. and Kim, K.-M.: The 2010 Pakistan flood and Russian heat wave: Teleconnection of hydrometeorological extremes, J Hydrometeorol., 13, 392–403, https://doi.org/10.1175/JHM-D-11-016.1, 2012.

Lucarini, V. and Gritsun, A.: A new mathematical framework for atmospheric blocking events, Clim. Dyn., 54, 575–598, https://doi.org/10.1007/s00382-019-05018-2, 2020.

Ma, Q. and Franzke, C. L. E.: The role of transient eddies and diabatic heating in the maintenance of European heat waves: a nonlinear quasi-stationary wave perspective, Clim. Dyn., 56, 2983 – 3002, https://doi.org/10.1007/s00382-021-05628-9, 2021.

Nakamura, N. and Huang, C. S.: Atmospheric blocking as a traffic jam in the jet stream, Science, 361, 42–47, https://doi.org/10.1126/science.aat0721, 2018.

Park, M. and Lee, S.: Relationship between tropical and extratropical diabatic heating and their impact on stationary–transient wave interference, J Atmos Sci, 76, 2617–2633, https://doi.org/10.1175/JAS-D-18-0371.1, 2019.

Perron, M. and Sura, P.: Climatology of non-Gaussian atmospheric statistics, J. Clim., 26, 1063–1083, https://doi.org/10.1175/JCLI-D-11-00504.1, 2013.

Petoukhov, V., Rahmstorf, S., Petri, S., and Schellnhuber, H. J.: Quasiresonant amplification of planetary waves and recent Northern Hemisphere weather extremes, Proc. Natl. Acad. Sci. U.S.A., 110, 5336–5341, https://doi.org/10.1073/pnas.1222000110, 2013.

Ragone, F. and Bouchet, F.: Rare Event Algorithm Study of Extreme Warm Summers and Heatwaves Over Europe, Geophys. Res. Lett.s, 48, https://doi.org/10.1029/2020gl091197, 2021.

Rienecker, M. M., Suarez, M. J., Gelaro, R., Todling, R., Bacmeister, J., Liu, E., Bosilovich, M. G., Schubert, S. D., Takacs, L., Kim, G.-K., Bloom, S., Chen, J., Collins, D., Conaty, A., da Silva, A., Gu, W., Joiner, J., Koster, R. D., Lucchesi, R., Molod, A., Owens, T., Pawson, S., Pegion, P., Redder, C. R., Reichle, R., Robertson, F. R., Ruddick, A. G., Sienkiewicz, M., and Woollen, J.: MERRA: NASA's Modern-Era Retrospective Analysis for Research and Applications, Journal of Climate, 24, 3624 – 3648, https://doi.org/10.1175/JCLI-D-11-00015.1, 2011.

Rogers, C. D.: Inverse Methods for Atmospheric Sounding: Theory and Practice, Series on Atmospheric, Oceanic and Planetary Physics, World Scientific Publ., Singapore, 2000.

Rousi, E., Kornhuber, K., Beobide-Arsuaga, G., Luo, F., and Coumou, D.: Accelerated western European heatwave trends linked to more-persistent double jets over Eurasia, Nat Commun, 13, 3851, https://doi.org/https://doi.org/10.1038/s41467-022-31432-y, 2022.

Schneidereit, A., Schubert, S., Vargin, P., Lunkeit, F., Zhu, X., Peters, D. H., and Fraedrich, K.: Large-scale flow and the long-lasting blocking high over Russia: Summer 2010, Mon Weather Rev., 140, 2967–2981, https://doi.org/10.1175/MWR-D-11-00249.1, 2012.

Screen, J. A. and Simmonds, I.: Amplified mid-latitude planetary waves favour particular regional weather extremes, Nat. Clim. Change, 4, 704–709, https://doi.org/10.1038/nclimate2271, 2014.

Shutts, G.: The propagation of eddies in diffluent jetstreams: Eddy vorticity forcing of 'blocking'flow fields, Q. J. R. Meteorol. Soc., 109, 737–761, https://doi.org/10.1002/qj.49710946204, 1983.

Stefanon, M., D'Andrea, F., and Drobinski, P.: Heatwave classification over Europe and the Mediterranean region, Environ. Res. Lett., 7, 014 023, https://doi.org/10.1088/1748-9326/7/1/014023, 2012.

Sura, P., Newman, M., Penland, C., and Sardeshmukh, P.: Multiplicative noise and non-Gaussianity: A paradigm for atmospheric regimes?, J. Atmos. Sci., 62, 1391–1409, https://doi.org/10.1175/JAS3408.1, 2005.

Teng, H. and Branstator, G.: A zonal wavenumber 3 pattern of Northern Hemisphere wintertime planetary wave variability at high latitudes, J. Clim., 25, 6756–6769, https://doi.org/10.1175/JCLI-D-11-00664.1, 2012.

Teng, H. and Branstator, G.: Amplification of Waveguide Teleconnections in the Boreal Summer, Curr. Clima. Change Rep., 5, 421 – 432, https://doi.org/10.1007/s40641-019-00150-x, 2019.

Trenberth, K. E. and Fasullo, J. T.: Climate extremes and climate change: The Russian heat wave and other climate extremes of 2010, J. Geophys. Res. Atmos., 117, https://doi.org/10.1029/2012JD018020, 2012.

Žagar, N., Kasahara, A., Terasaki, K., Tribbia, J., and Tanaka, H.: Normal-mode function representation of global 3D datasets: open-access software for the atmospheric research community, Geosci. Model Dev., 8, 1169–1195, https://doi.org/https://doi.org/10.5194/gmd-8-1169-2015, 2015.

Wiedenmann, J. M., Lupo, A. R., Mokhov, I. I., and Tikhonova, E. A.: The climatology of blocking anticyclones for the Northern and Southern Hemispheres: Block intensity as a diagnostic, J. Clim., 15, 3459–3473, https://doi.org/10.1175/1520-0442(2002)015<3459:TCOBAF>2.0.CO;2", 2002.

Wilks, D. S.: Statistical methods in the atmospheric sciences, vol. 100 of *International Geophysics*, Academic Press, third edn., http://www.sciencedirect.com/science/bookseries/00746142/100/supp/C, 2011.

Wirth, V. and Polster, C.: The problem of diagnosing jet waveguidability in the presence of large-amplitude eddies, J. Atmos. Sci., 78, 3137–3151, https://doi.org/10.1175/JAS-D-20-0292.1, 2021.

Woollings, T., Barriopedro, D., Methven, J., Son, S.-W., Martius, O., Harvey, B., Sillmann, J., Lupo, A. R., and Seneviratne, S.: Blocking and its response to climate change, Curr. Clima. Change Rep., 4, 287–300, https://doi.org/10.1007/s40641-018-0108-z, 2018.

Xu, P., Wang, L., Liu, Y., Chen, W., and Huang, P.: The record-breaking heat wave of June 2019 in Central Europe, Atmos. Sci. Lett., 21, e964, https://doi.org/10.1002/asl.964, 2020.

Yamazaki, A. and Itoh, H.: Vortex–vortex interactions for the maintenance of blocking. Part I: The selective absorption mechanism and a case study, J. Atmos. Sci., 70, 725–742, https://doi.org/10.1175/JAS-D-11-0295.1, 2013.

Žagar, N., Jelić, D., Blaauw, M., and Bechtold, P.: Energy spectra and inertia–gravity waves in global analyses, J. Atmos. Sci., 74, 2447–2466, https://doi.org/10.1175/JAS-D-16-0341.1, 2017.

Žagar, N., Kosovelj, K., Manzini, E., Horvat, M., and Castanheira, J.: An assessment of scale-dependent variability and bias in global prediction models, Clim. Dyn., 54, 287–306, https://doi.org/10.1007/s00382-019-05001-x, 2019.

Žagar, N., Zaplotnik, Ž., and Karami, K.: Atmospheric subseasonal variability and circulation regimes: spectra, trends, and uncertainties, J. Clim., 33, 9375–9390, https://doi.org/10.1175/JCLI-D-20-0225.1, 2020.

Zhou, Y. and Wu, Z.: Possible impacts of mega-El Niño/Southern Oscillation and Atlantic Multidecadal Oscillation on Eurasian heatwave frequency variability, Q. J. R. Meteorol. Soc., 142, 1647–1661, https://doi.org/10.1002/qj.2759, 2016.